

# Transition from Fireball to Poynting-flux-dominated Outflow in Three-Episode GRB 160625B

B.-B. Zhang<sup>1,2,3</sup>, B. Zhang<sup>4</sup>, A. J. Castro-Tirado<sup>1,5</sup>, Z. G. Dai<sup>2,6</sup>, P.-H. T. Tam<sup>7</sup>, X.-Y. Wang<sup>2,6</sup>, Y.-D. Hu<sup>1,8</sup>, S. Karpov<sup>9,10</sup>, A. Pozanenko<sup>11,12</sup>, F.-W. Zhang<sup>13</sup>, E. Mazaeva<sup>11</sup>, P. Minaev<sup>11</sup>, A. Volnova<sup>11</sup>, S. Oates<sup>32</sup>, H. Gao<sup>14</sup>, X.-F. Wu<sup>15,16,17</sup>, L. Shao<sup>18,15</sup>, Q.-W. Tang<sup>35,6</sup>, G. Beskin<sup>9,10</sup>, A. Biryukov<sup>19,10</sup>, S. Bondar<sup>20</sup>, E. Ivanov<sup>20</sup>, E. Katkova<sup>20</sup>, N. Orekhova<sup>20</sup>, A. Perkov<sup>20</sup>, V. Sasyuk<sup>10</sup>, L. Mankiewicz<sup>21</sup>, A. F. Żarnecki<sup>22</sup>, A. Cwiek<sup>23</sup>, R. Opiela<sup>21</sup>, A. Zadrożny<sup>23</sup>, R. Aptekar<sup>24</sup>, D. Frederiks<sup>24</sup>, D. Svinkin<sup>24</sup>, A. Kusakin<sup>25</sup>, R. Inasaridze<sup>26</sup>, O. Burhonov<sup>27</sup>, V. Rumyantsev<sup>28</sup>, E. Klunko<sup>29</sup>, A. Moskvitin<sup>9</sup>, T. Fatkhullin<sup>9</sup>, V. V. Sokolov<sup>9</sup>, A. F. Valeev<sup>9,10</sup>, S. Jeong<sup>1,30</sup>, I. H. Park<sup>30</sup>, M. D. Caballero-García<sup>31</sup>, R. Cunniffe<sup>1</sup>, J. C. Tello<sup>1</sup>, P. Ferrero<sup>1</sup>, S. B. Pandey<sup>33</sup>, M. Jelínek<sup>31</sup>, R. Sánchez-Ramírez<sup>1</sup>, A. Castellón<sup>34</sup>

The ejecta composition of gamma-ray bursts (GRBs) is an open question in GRB physics [1]. Some GRBs possess a quasi-thermal spectral component in the time-resolved spectral analysis [2, 3], suggesting a hot fireball origin. Some others show an essentially feature-less non-thermal spectrum known as the “Band” function [4, 5], which can be interpreted as synchrotron radiation in an optically thin region [5, 6], suggesting a Poynting-flux-dominated jet composition [7]. Here we report an extraordinarily bright GRB 160625B, simultaneously observed in gamma-rays and optical wavelengths, whose prompt emission consists of three dramatically different isolated episodes separated by long quiescent intervals, with the durations of each “sub-burst” being  $\sim 0.8$  s, 35 s, and 212 s, respectively. The high brightness (with isotropic peak luminosity  $L_{\text{p,iso}} \sim 4 \times 10^{53}$  erg/s) of this GRB allows us to conduct detailed time-resolved spectral analysis in each episode, from precursor to the main burst and extended emission. Interestingly, the spectral properties of the first two sub-bursts are distinctly different, which allow us for the first time to observe the transition from thermal to non-thermal radiation in a single GRB. Such a transition is a clear indication of the change of jet composition from a fireball to a Poynting-flux-dominated jet.

<sup>1</sup>Instituto de Astrofísica de Andalucía (IAA-CSIC), P.O. Box 03004, E-18080 Granada, Spain; zhang.grb@gmail.com; <sup>2</sup>School of Astronomy and Space Science, Nanjing University, Nanjing 210093, China; <sup>3</sup>Scientist Support LLC, Madison, AL 35758, USA; <sup>4</sup>Department of Physics and Astronomy, University of Nevada, Las Vegas, NV 89154, USA; <sup>5</sup>Departamento de Ingeniería de Sistemas y Automática, Escuela de Ingenierías, Universidad de Málaga, C. Dr. Ortiz Ramos sn, 29071 Málaga, Spain; <sup>6</sup>Key laboratory of Modern Astronomy and Astrophysics (Nanjing University), Ministry of Education, Nanjing 210093, China; <sup>7</sup>School of Physics and Astronomy, Sun Yat-Sen University, Zhuhai 519082, China; <sup>8</sup>Universidad de Granada, Facultad de Ciencias Campus Fuentenueva s/n E-18071 Granada, Spain; <sup>9</sup>Special Astrophysical Observatory of Russian Academy of Sciences, Nizhniy Arkhyz, Russia; <sup>10</sup>Kazan Federal University, Kazan, Russia; <sup>11</sup>Space Research Institute of the Russian Academy of Sciences, 117997, Russia, Moscow, Profsoyuzanaya, 84/32; <sup>12</sup>National Research Nuclear University MEPhI (Moscow Engineering Physics Institute), 115409, Russia, Moscow, Kashirskoe shosse, 31; <sup>13</sup>College of Science, Guilin University of Technology, Guilin 541004, China; <sup>14</sup>Department of Astronomy, Beijing Normal University, Beijing 100875, China; <sup>15</sup>Purple Mountain Observatory, Chinese Academy of Sciences, Nanjing 210008, China; <sup>16</sup>School of Astronomy and Space Science, University of Science and Technology of China, Hefei, Anhui 230026, China; <sup>17</sup>Joint Center for Particle, Nuclear Physics and Cosmology, Nanjing University-Purple Mountain Observatory, Nanjing 210008, China; <sup>18</sup>Department of Space Sciences and Astronomy, Hebei Normal University, Shijiazhuang 050024, China; <sup>19</sup>Moscow State University, Moscow, Russia; <sup>20</sup>Research and Production Corporation “Precision Systems and Instruments”, Nizhniy Arkhyz, Russia; <sup>21</sup>Center for Theoretical Physics PAS, Al. Lotnikow 32/46, 02-668 Warsaw, Poland; <sup>22</sup>Faculty of Physics, University of Warsaw, Pasteura 5, 02-093 Warsaw, Poland; <sup>23</sup>National Centre for Nuclear Research, Hoża 69, 00-681 Warsaw, Poland; <sup>24</sup>Ioffe Institue, Politekhnikeskaya ul., 26, St. Petersburg, 194021, Russia; <sup>25</sup>Fesenkov Astrophysical Institute, Kazakhstan, Almaty, 050020, 23; <sup>26</sup>Kharadze Abastumani Astrophysical Observatory, Ilia State University, Georgia, Tbilisi, 0162, Kakutsa Cholokashvili Ave 3/5; <sup>27</sup>Ulugh Beg Astronomical Institute, Uzbekistan, 100052, Tashkent, Astronomicheskaya st., 33; <sup>28</sup>Crimean Astrophysical Observatory, 298409, Crimea, Nauchny, Ukraina; <sup>29</sup>Institute of Solar-Terrestrial Physics, 664033, Russia, Irkutsk p/o box 291; Lermontov st., 126a <sup>30</sup>Department of Physics, Sungkyunkwan University (SKKU), Suwon, 440-746 Korea; <sup>31</sup>Astronomical Institute of the Academy of Sciences, Bocni II 1401, CZ-141 00 Praha 4 – Sporilov, Czech Republic; <sup>32</sup>Department of Physics, University of Warwick, Coventry, CV4 7AL, UK; <sup>33</sup>ARIES, Manora Peak, Nainital, India; <sup>34</sup>Departamento de Álgebra, Geometría y Topología, Facultad de Ciencias, Universidad de Málaga, C. Juan López Peñalver, sn, 29071 Málaga, Spain; <sup>35</sup>School of Science, Nanchang University, Nanchang 330031, China

A relativistic GRB outflow can be either matter-dominated or magnetically dominated.

One diagnostic test of such composition is the observed spectrum. If it is a matter-dominated “fireball”, a bright quasi-thermal spectral component is expected, usually accompanied with a non-thermal component originated from the internal shocks [8–10]. Indeed, such a quasi-thermal component, usually characterized as a multi-temperature blackbody in the time-integrated spectra and a Planck-like function in the time-resolved spectra, has been observed in a few cases (e.g, GRB 090902B) [2, 3]. If the outflow is magnetically dominated, the photosphere component would be suppressed so that the observed spectrum is dominated by a non-thermal synchrotron emission component [7]. Some GRBs indeed show synchrotron-only spectra without evidence of a thermal component (e.g. GRB 130427A and GRB 130606B) [5, 11]. The cases with superposition of a sub-dominant thermal component on a dominant synchrotron component are also observed (e.g. GRB 100724B, GRB 110721A, and GRB 120323A) [12, 13], which can be understood if GRBs have a hybrid jet composition [14]. However, no significant change of jet composition has been observed in a single GRB in the past.

GRB 160625B triggered Gamma-Ray Monitor (GBM; 8 keV - 40 MeV) on board the NASA *Fermi* Gamma-Ray Observatory twice at 22:40:16.28 UT and 22:43:24.82 on 25 June 2016 [15]. Its intense high-energy photon flux also triggered the Large Area Telescope (LAT) on board *Fermi*, *Konus-Wind*, *INTEGRAL*/SPI-ACS and CALET (attached to the *ISS*). The prompt emission light curves and spectral fitting results are shown in Figure 1. Long term follow-up observations of the burst have been carried out by *Swift* and several ground-based optical telescopes (see Supplementary Information for the details). The overall long term multi-wavelength afterglow light curves are presented in Figure 2. A summary of the timing and spectral properties of the burst are listed in Table I.

One distinct feature of GRB 160625B is that it is composed of three sub-bursts separated by two quiescent times ( $\sim 180$  s and  $\sim 339$  s, respectively). The first sub-burst, which is undoubtedly related to the main event (see Supplementary Figure 1) is particularly interesting as it’s short duration ( $\sim 0.84$  s) gives it the appearance of a traditional short GRB (Figure 1). To test such a possibility, we over-plot all the three sub-bursts on the  $E_p - E_{\text{iso}}$  and  $E_p - L_{\text{p,iso}}$  diagrams in Figure 3, where  $E_p$  is peak energy in the  $\nu F\nu$  energy spectrum,  $E_{\text{iso}}$  is isotropic equivalent radiated energy and  $L_{\text{p,iso}}$  is the isotropic peak luminosity. The values of  $E_p$  in Figure 3 are from the time-integrated spectral fitting using a Band function or cutoff power law model, which are listed in Table 1. It can be seen that all three

sub-bursts lie in the long GRB tracks in both diagrams. According to the multi-wavelength physical classification criteria flowchart (Figure 8 of [16]), all three sub-bursts fall into the correlations of Type II (massive star origin) rather than Type I (compact star origin) GRB category. On the other hand, a good fraction of long GRBs show a short precursor before the main emission episode [17]. The first sub-burst in our analysis is consistent with being a precursor of the main burst.

Most interestingly, the time-resolved spectral shape of the first sub-burst is a typical blackbody function. As shown in Supplementary Table I and Supplementary Figure 3, the Planck function gives an adequate fit to the time-resolved spectra in 6 fine time bins with satisfactory goodness of fit. We note that a power-law with a high-energy exponential cutoff model can also give acceptable/improved fit. The Planck function was chosen because it carries a physical meaning. A few GRBs have shown a thermal precursor before [18]. However, GRB 160625B for the first time allows one to perform a fine time-resolved spectral analysis and track the blackbody evolution. Based on the standard fireball photosphere model [20], one can infer the fireball launch radius  $r_0 Y^{3/2}$  and the bulk Lorentz factor  $\Gamma Y^{-1/4}$ , where  $Y > 1$  is the ratio between total energy of the fireball and the energy emitted in  $\gamma$ -rays at the photosphere. The derived values are also presented in Supplementary Table I, which suggests a highly relativistic fireball launched from a radius of a few  $\times 10^8$  cm, the range of a typical jet emerging from a Wolf-Rayet progenitor star [19].

The 2nd sub-burst is consistent with a typical long GRB with  $T_{90} \sim 35.1$  s. At redshift  $z = 1.406 \pm 0.001$  determined by our Gran Telescopio CANARIAS (GTC) observations (see Supplementary Figure 2), the derived total isotropic  $\gamma$ -ray energy is  $E_{\text{iso}} \sim 3 \times 10^{54}$  erg, making it the fifth most energetic GRB ever observed with known redshift. Thanks to its high flux, one can divide the 2nd sub-burst into 59 slices based on the criterion to have enough photons each bin to conduct a fine time-resolved spectral analysis. The length of each time bins are comparable to the ones used for the 1st sub-burst. The spectrum of each time slice cannot be fit with a Planck-like spectrum, but can be successfully fit by the Band function model[4]. The best-fit parameters are listed in Supplementary Table 1 and their evolution with time is plotted in Figure 1. Adding an additional thermal component neither improves the goodness of the fit, nor leads to constraints on the parameters of the new component (for details see Supplementary Figure 4). The  $E_p$  evolution first shows a hard-to-soft evolution trend during the time 180-190 s interval following the first trigger,

and then generally follows an intensity tracking pattern thereafter. All the Band-function parameters are typical and similar to most long GRBs. Physically, a typical GRB spectrum (e.g, with  $\alpha \sim -1$  and  $\beta \sim -2.2$  in the context of Band function fit) can be explained by synchrotron emission in a decaying magnetic field [6], and confronting the model to the data indeed suggests that such a model can fit the data equally well as the Band function [5]. We perform the synchrotron model as described in [5] to fit the time-dependent spectra of the second sub-burst and obtained satisfactory fits. One example of such fits is presented in Supplementary Figure 5. The non-existence of a thermal component in these time bins suggests a Poynting flux dominated outflow with the photosphere emission suppressed.

Although six times longer than the 2nd sub-burst, the 3rd sub-burst is the faintest among the three sub-bursts – about 126 times weaker than the 2nd sub-burst in term of peak flux (Table I). Due to low photon statistics, most time resolved spectra of the 3rd sub-bursts can be adequately fit by a simple power law model with the exception of two slices, in which a cutoff power law model is needed and  $E_p$  can be constrained (Supplementary Table I). The spectral evolution of the 3rd sub-burst is also shown in Figure 1.

LAT detected high-energy emission up to 15.3 GeV during the prompt emission of GRB 160625B. Supplementary Figure 6 displays the energy-dependent light curves of the three sub-bursts with the  $> 1$  GeV LAT photons plotted individually as a function of arrival time.

Optical observations (including the data presented here) using a dozen telescopes (see Supplementary Table II) were also carried out before the trigger of the first sub-burst, during the prompt and afterglow emission phases, which place deep upper limits during the quiescent phase between the first two sub-pulses and lead to detections during the 2nd sub-pulse. There is a  $\sim 3$  s lag between optical emission and the GBM band emission (Supplementary Figure 7).

The spectral energy distributions (SEDs) from optical to GeV band at three epochs during the 2nd-sub-burst are presented in Supplementary Figure 8. An immediate impression is that the optical emission is in excess of the extrapolation of sub-MeV spectral component to the optical band. A similar case was observed in the “naked-eye” GRB 080319B [21]. A possible explanation could be that the optical emission is due to the synchrotron radiation while the sub-MeV emission is due to the synchrotron-self-Compton (SSC) emission [21, 22]. However, such a model would predict a strong second-order SSC appearing in the GeV-TeV range [23]. The LAT emission is consistent with or even steeper than the extrapolation of

the sub-MeV emission to the GeV range, without evidence of the second SSC component. This disfavors the SSC origin of the sub-MeV component. Instead we interpret the sub-MeV emission as synchrotron emission in a magnetic dissipation region within the Poynting-flux-dominated outflow [6, 24]. The optical emission would be produced at a farther distance from the central engine, as suggested by the  $\sim 3$  s time delay. One possibility is the reverse shock emission as the variable moderately magnetized ejecta (after significant magnetic dissipation to produce the sub-MeV emission itself) catch up in the wake of the initial fireball blastwave. Alternatively, like in the “naked-eye” GRB 080319B, in which a similar  $\sim 2$  s delay was observed [25], the optical emission of GRB 160625B may have originated from residual internal shocks [26] or from free neutron decay at a large radius from the central engine [27].

The apparent change of jet composition between two emission episodes of GRB 160625B sheds light on the central engine of the GRB. The first sub-burst is likely associated with the initial iron core collapse that forms a black hole or a rapidly spinning magnetar surrounded by some high-angular momentum materials. The initial hyper-accretion onto the central object forms a matter-dominated fireball via neutrino-anti-neutrino ( $\nu - \bar{\nu}$ ) annihilations. The jet may be intermittent, but lasts longer than the duration for the jet to penetrate through the star. The first several pulses within the ejecta merge and eventually break out of the star to make a successful thermally-dominant GRB precursor [28]. After the early prompt accretion phase, the central engine enters a quiescent phase lasting for  $\sim 180$  s. This could be due to one of the following reasons: 1). In the context of the black hole central engine model, the accretion may be halted by a magnetic barrier from the central engine [29] after the initial prompt accretion phase. One needs to wait to accumulate enough materials to break through the barrier. The free-fall time scale of the C/O core is  $\sim 100$  s, which may be related to the waiting time before the magnetic barrier is broken [28]. 2). In the context of the magnetar central engine model, after the initial accretion phase, the proto-magnetar would need to take some time to cool before a Poynting-flux-dominated outflow is launched [30]. The cooling time scale is typically 10s of seconds, somewhat shorter than the quiescent period. However, the competition between fall-back spin-up and magnetic spin-down may delay the launch of the outflow. In both above-mentioned scenarios, the central engine is strongly magnetized when the second jet is launched, so that the emission would be characterized by a synchrotron spectrum without a significant thermal component from

the photosphere. After the main emission episode (the second sub-burst), the central engine would reactivate again similar to the GRBs that show significant late-time X-ray flares [31], which powers the third emission episode (the second sub-burst).

Some GRBs have a precursor, while some others are characterized by extended X-ray flare emission. GRB 160625B consists of three distinct emission episodes which may correspond to the precursor, main burst, and delayed X-ray flare, respectively. Thanks to its exceptional brightness, one was able to study the detailed spectral evolution of the three episodes in detail. If the burst was less energetic or was placed at a larger distance, one would only detect two episodes or even only one, and the event would be ascribed as a “normal” GRB. It is possible that GRB 160625B is the proto-type of at least one sub-group of long GRBs, which display three distinct emission episodes [17], and the physical processes delineated in this paper may apply to these bursts in general.

## References

---

1. Kumar, P., & Zhang, B., The physics of gamma-ray bursts & relativistic jets, *Physics Reports*. **561**, 1, (2015)
2. Ryde, F., et al., Identification and Properties of the Photospheric Emission in GRB090902B, *The Astrophysical Journal*. **709**, L172, (2010)
3. Zhang, B.-B., et al., A Comprehensive Analysis of Fermi Gamma-ray Burst Data. I. Spectral Components and the Possible Physical Origins of LAT/GBM GRBs, *The Astrophysical Journal*. **730**, 141, (2011)
4. Band, D., et al., BATSE observations of gamma-ray burst spectra. I - Spectral diversity, *Astrophys. J.* **413**, 281, (1993)
5. Zhang, B.-B., Uhm, Z. L., Connaughton, V., Briggs, M. S., & Zhang, B., Synchrotron Origin of the Typical GRB Band Function - A Case Study of GRB 130606B, *The Astrophysical Journal*. **816**, 72, (2016)
6. Uhm, Z. L., & Zhang, B., Fast-cooling synchrotron radiation in a decaying magnetic field and  $\gamma$ -ray burst emission mechanism, *Nature Physics*. **10**, 351, (2014)
7. Zhang, B., & Pe’er, A., Evidence of an Initially Magnetically Dominated Outflow in GRB

- 080916C, *The Astrophysical Journal*. **700**, L65, (2009)
8. Paczynski, B., Gamma-ray bursters at cosmological distances, *The Astrophysical Journal*. **308**, L43, (1986)
  9. Goodman, J., Are gamma-ray bursts optically thick?, *The Astrophysical Journal*. **308**, L47, (1986)
  10. Mészáros, P., & Rees, M. J., Steep Slopes and Preferred Breaks in Gamma-Ray Burst Spectra: The Role of Photospheres and Comptonization, *The Astrophysical Journal*. **530**, 292, (2000)
  11. Preece, R., et al., The First Pulse of the Extremely Bright GRB 130427A: A Test Lab for Synchrotron Shocks, *Science*. **343**, 51, (2014)
  12. Axelsson, M., et al., GRB110721A: An Extreme Peak Energy and Signatures of the Photosphere, *The Astrophysical Journal*. **757**, L31, (2012)
  13. Guiriec, S., et al., Evidence for a Photospheric Component in the Prompt Emission of the Short GRB 120323A and Its Effects on the GRB Hardness-Luminosity Relation, *The Astrophysical Journal*. **770**, 32, (2013)
  14. Gao, H., & Zhang, B., Photosphere Emission from a Hybrid Relativistic Outflow with Arbitrary Dimensionless Entropy and Magnetization in GRBs, *The Astrophysical Journal*. **801**, 103, (2015)
  15. Burn, E. GRB 160625B: Fermi GBM initial observations., *GRB Coordinates Network*, **19581**, 1, (2016)
  16. Zhang, B., et al., Discerning the Physical Origins of Cosmological Gamma-ray Bursts Based on Multiple Observational Criteria: The Cases of  $z = 6.7$  GRB 080913,  $z = 8.2$  GRB 090423, and Some Short/Hard GRBs, *The Astrophysical Journal*. **703**, 1696, (2009)
  17. Hu, Y.-D., Liang, E.-W., Xi, S.-Q., Peng, F.-K., Lu, R.-J., Lü, L.-Z., & Zhang, B., Internal Energy Dissipation of Gamma-Ray Bursts Observed with Swift: Precursors, Prompt Gamma-Rays, Extended Emission, and Late X-Ray Flares, *The Astrophysical Journal*. **789**, 145, (2014)
  18. Murakami, T., Inoue, H., Nishimura, J., van Paradijs, J., & Fenimore, E. E., A gamma-ray burst preceded by X-ray activity, *Nature*. **350**, 592, (1991)
  19. Castro-Tirado, A. J., et al., GRB 021004: Tomography of a gamma-ray burst progenitor and its host galaxy, *Astronomy and Astrophysics*. **517**, A61, (2010)
  20. Pe'er, A., Ryde, F., Wijers, R. A. M. J., Mészáros, P., & Rees, M. J., A New Method of Determining the Initial Size and Lorentz Factor of Gamma-Ray Burst Fireballs Using a Thermal



- Emission Component, *The Astrophysical Journal* **664**, L1, (2007)
21. Racusin, J. L., et al., Broadband observations of the naked-eye  $\gamma$ -ray burst GRB080319B, *Nature*. **455**, 183, (2008)
  22. Kumar, P., & Panaitescu, A., What did we learn from gamma-ray burst 080319B?, *Monthly Notices of the Royal Astronomical Society*. **391**, L19, (2008)
  23. Piran, T., Sari, R., & Zou, Y.-C., Observational limits on inverse Compton processes in gamma-ray bursts, *Monthly Notices of the Royal Astronomical Society*. **393**, 1107, (2009)
  24. Zhang, B., & Yan, H., The Internal-collision-induced Magnetic Reconnection and Turbulence (ICMART) Model of Gamma-ray Bursts, *The Astrophysical Journal*. **726**, 90, (2011)
  25. Beskin, G., Karpov, S., Bondar, S., Greco, G., Guarnieri, A., Bartolini, C., & Piccioni, A., Fast Optical Variability of a Naked-eye Burst—Manifestation of the Periodic Activity of an Internal Engine, *The Astrophysical Journal*. **719**, L10, (2010)
  26. Li, Z., & Waxman, E., Prompt Optical Emission from Residual Collisions in Gamma-Ray Burst Outflows, *The Astrophysical Journal*. **674**, L65, (2008)
  27. Fan, Y.-Z., Zhang, B., & Wei, D.-M., Naked-eye optical flash from gamma-ray burst 080319B: Tracing the decaying neutrons in the outflow, *Physical Review D*. **79**, 021301, (2009)
  28. Wang, X.-Y., & Mészáros, P., GRB Precursors in the fallback Collapsar Scenario, *The Astrophysical Journal*. **670**, 1247, (2007)
  29. Proga, D., & Zhang, B., The late time evolution of gamma-ray bursts: ending hyperaccretion and producing flares, *Monthly Notices of the Royal Astronomical Society*. **370**, L61, (2006)
  30. Metzger, B. D., Giannios, D., Thompson, T. A., Bucciantini, N., & Quataert, E., The protomagnetar model for gamma-ray bursts, *Monthly Notices of the Royal Astronomical Society*. **413**, 2031, (2011)
  31. Burrows, D. N., et al., Bright X-ray Flares in Gamma-Ray Burst Afterglows, *Science*. **309**, 1833, (2005)

## Acknowledgments

BBZ thank Y.-Z. Fan, Y.-Z. Wang, H. Wang, K. D. Alexander and D. Lazzati for helpful discussions. We are grateful to K. Hurley, I. Mitrofanov, A. Sanin, M. Litvak, and W. Boynton for the use of *Mars Odyssey* data in the triangulation. We acknowledge the use of the public data from the *Swift* and *Fermi* data archives. BBZ and AJCT acknowledge

support from the Spanish Ministry Projects AYA 2012-39727-C03-01 and AYA2015-71718-R. Part of this work made use of BBZ's personal IDL code library ZBBIDL and personal Python library ZBBPY. The computation resources used in this work are owned by Scientist Support LLC. BZ acknowledges NASA NNX14AF85G and NNX15AK85G for support. ZGD acknowledges the National Natural Science Foundation of China (grant No. 11573014). YDH acknowledges the support by China Scholarships Council(CSC) under the Grant No.201406660015. Mini-MegaTORTORA belongs to Kazan Federal University and the work is performed according to the Russian Government Program of Competitive Growth of Kazan Federal University. AP, EM, PM and AV are grateful to Russian Science Foundation (grant 15-12-30016) for support. RI is grateful to the grant RUSTAVELI FR/379/6-300/14 for a partial support. Observations on Mini-MegaTORTORA are supported by the Russian Science Foundation grant No. 14-50-00043. VAF and MAS are thankful to the Russian Science Foundation (grant 14-50-00043). LM and AFZ acknowledge support from INTA-CEDEA ESAt personnel hosting the Pi of the Sky facility at the BOOTES-1 station. HG acknowledges the National Natural Science Foundation of China under grants 11603003. XYW acknowledges the National Natural Science Foundation of China under grant 11625312. ZGD, XFW, BZ, XYW, LS and FWZ are also supported by the 973 program under grant 2014CB845800. FWZ is also supported in part by NSFC under grants No. U1331101 and No. 11163003 and by the Guangxi Natural Science Foundation (No. 2013GXNSFAA019002) and by the project of outstanding young teachers' training in higher education institutions of Guangxi. LS acknowledges the support by the National Natural Science Foundation of China (No. 11103083) and the Joint NSFC-ISF Research Program (No. 11361140349). SRO acknowledges the support of the Leverhulme Trust. SJ acknowledges the support from Korea Basic Science Research Program through NRF-2014R1A6A3A03057484 and NRF-2015R1D1A4A01020961, and IHP from National Research Foundation grants of No. 2015R1A2A1A01006870 and No. 2015R1A2A1A15055344. RA gratefully acknowledges support from RFBR grants 15-02-00532-i and 16-29-13009-ofi-m.

### **Authors Contributions**

## METHODS

**Data Reduction and Spectral Fitting** We processed the GBM and LAT data using the standard software as described in [3] and [5]. The data from the two brightest Sodium Iodide (NaI) scintillation detectors and the brightest Bismuth Germanate (BGO) scintillation detectors on board *Fermi* are used for our spectral fitting analysis. The task of spectral fitting is performed using our software package, *McSpecFit*, which combines a Bayesian MC engine *McFit*, general forward-folding codes and likelihood calculations and can fit any models to the observed spectra. In particular, the Bayesian Monte-Carlo engine (*McFit*), as described in [5, 32], employs a Bayesian Monte-Carlo (MC) fitting technique to reliably fit parameters that are constrained by the data even when other parameters are unconstrained. Using this technique, the best-fit parameters and their uncertainties can be realistically determined by the converged MC chains. The general forward-folding codes are used to compare a theoretical spectral model to data. In general, one needs to convolve the model with instrumental response, the Detector Response Matrix (DRM), to compare the models with the observational data. A general-purpose forward-folding code has been written [5] and it can handle the instrument response  $R(I, E)$  from any mission (e.g. *Fermi*/GBM), read in any model spectrum,  $F(E, P)$ , regardless of its form, and calculate the model-predicted count spectrum  $C_M(I, P) = \int_0^\infty F(E, P)R(I, E)dE$ . Such  $C_{M(I,P)}$  can be directly compared with the observed count spectrum  $C(I)$ . We then calculate the likelihood for those  $C_M(I, P)$  and  $C(I)$  pairs. In this paper, we use the maximum likelihood-based statistics, the so-called PGSTAT, for Poisson data, given by [33], but assuming the background to be Gaussian (see also <https://heasarc.gsfc.nasa.gov/xanadu/xspec/>). Such a likelihood function is then input into our fitting engine *McFit* so that the parameter space can be explored.

**Data Availability** The original *Fermi* observational data are available on-line in Fermi catalog [34] at <http://heasarc.gsfc.nasa.gov/FTP/fermi/data/gbm/bursts/>. The optical observational data used in this paper are available in Supplementary Table II. The detailed spectral fitting results are presented in Supplementary Table I. The short and long GRB samples presented in Figure 3 are taken from [35, 36].

TABLE I: Properties of Three Sub-bursts in GRB 160625B.

Sub-burst	A	B	C
$T_{90}$ [s] (15 - 350 keV )	$0.84^{+0.03}_{-0.01}$	$35.10^{+0.13}_{-0.23}$	$212.22^{+0.95}_{-2.27}$
waiting time [s]	-	$\sim 180$	$\sim 339$
lag (15 - 25 : 50 - 150 keV)	$0.007 \pm 0.013$	$0.80 \pm 0.05$	$-0.06 \pm 0.30$
$E_p$ (keV) (time-integrated)	$66.8 \pm 1.8$	$448.8^{+4.42}_{-4.22}$	$290.5^{+95.0}_{-55.7}$
fluence (erg cm $^{-2}$ )	$1.75 \pm 0.05 \times 10^{-6}$	$6.01 \pm 0.02 \times 10^{-4}$	$5.65 \pm 0.02 \times 10^{-5}$
$F_p$ (erg cm $^{-2}$ s $^{-1}$ )	$2.42 \pm 0.11 \times 10^{-6}$	$7.31 \pm 0.13 \times 10^{-5}$	$5.80 \pm 0.13 \times 10^{-7}$
$E_{\text{iso}}$ (erg)	$8.86 \pm 0.24 \times 10^{51}$	$3.05 \pm 0.01 \times 10^{54}$	$2.87 \pm 0.01 \times 10^{53}$
$L_{p,\text{iso}}$ (erg s $^{-1}$ )	$1.23 \pm 0.05 \times 10^{52}$	$3.71 \pm 0.06 \times 10^{53}$	$2.94 \pm 0.07 \times 10^{51}$
$z$	$1.406 \pm 0.001$		
Most energetic LAT photons	15.3 GeV (346.2 s); 6.95 GeV (793 s); 5.4 GeV (573 s)		

- 
32. Zhang, B.-B., van Eerten, H., Burrows, D. N., Ryan, G. S., Evans, P. A., Racusin, J. L., Troja, E., & MacFadyen, A., An Analysis of Chandra Deep Follow-up Gamma-Ray Bursts: Implications for Off-axis Jets, *The Astrophysical Journal*. **806**, 15, (2015)
33. Cash, W., Parameter estimation in astronomy through application of the likelihood ratio, *The Astrophysical Journal*. **228**, 939, (1979)
34. Narayana Bhat, P., et al., The Third Fermi GBM Gamma-Ray Burst Catalog: The First Six Years, *The Astrophysical Journal Supplement Series*. **223**, 28, (2016)
35. Zhang, F.-W., Shao, L., Yan, J.-Z., & Wei, D.-M., Revisiting the Long/Soft-Short/Hard Classification of Gamma-Ray Bursts in the Fermi Era, *The Astrophysical Journal*. **750**, 88, (2012)
36. Zhang, F.-W., Zhang, B., & Zhang, B., GRB 150906B - NGC 3313 association: Constraints from Ep-Eiso and Ep-Liso Relations., *GRB Coordinates Network*. **18298**, 1, (2015)

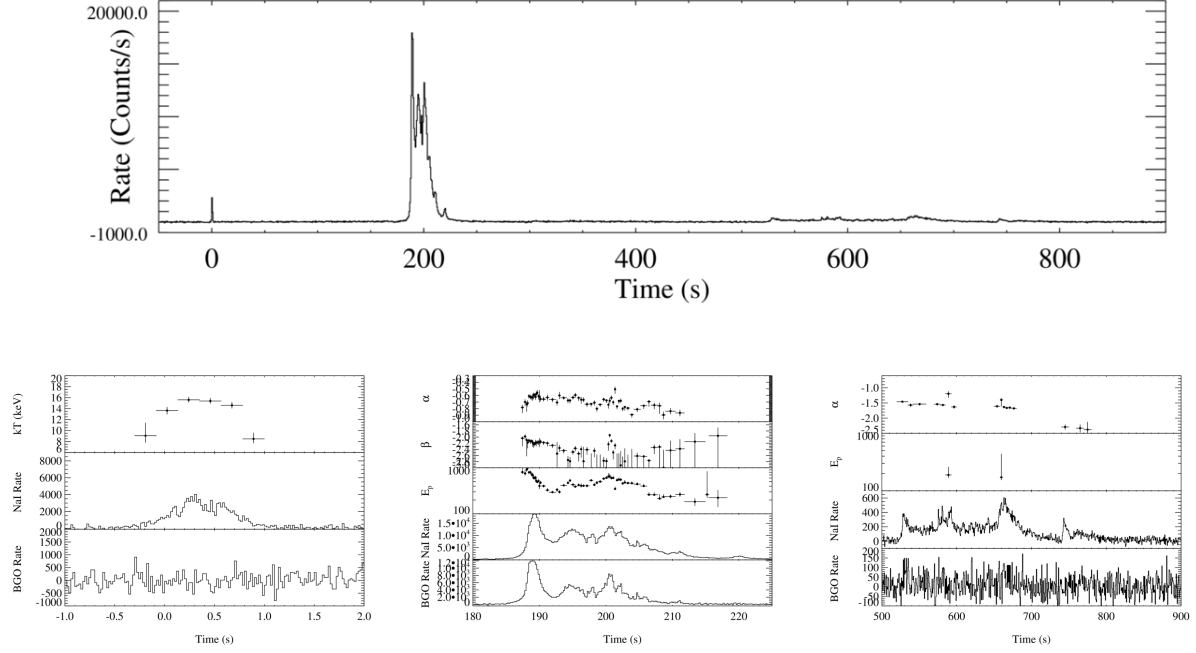


**Figure 1:** *Top:* prompt *Fermi*/GBM light curve of GRB 160625B. *Bottom:* Spectral evolution of three sub-bursts. Bottom two panels show the NaI and BGO light curves. The evolution of model parameters are displayed in the higher panels. The spectral models are blackbody, Band function, respectively, for the 1st and 2nd sub-bursts. For the 3rd sub-burst, a power law model is applied except two slices for which a power-law model with exponential cutoff is applied and  $E_p$  is constrained.

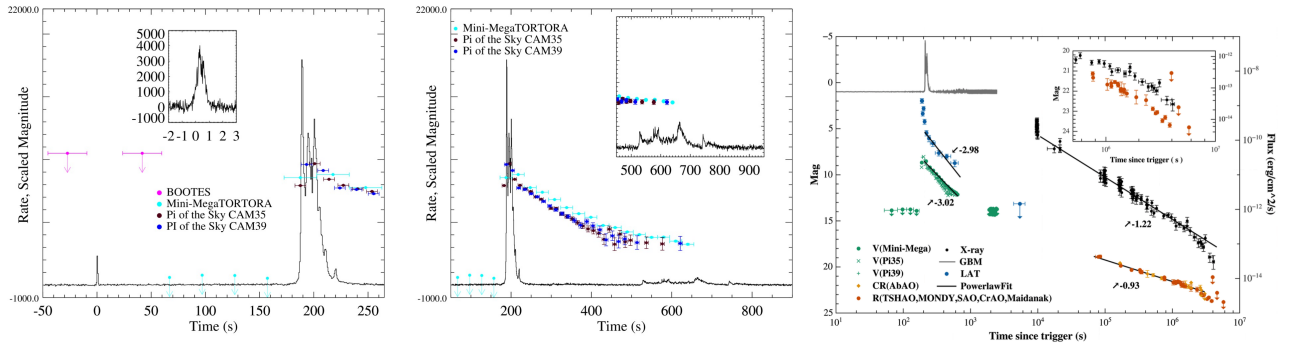


**Figure 2:** *Left two panels:* Optical Observations of the BOOTES-1, BOOTES-2, Pi of the Sky and MiniMega telescopes during the prompt emission in comparison with the GRB 160625B  $\gamma$ -ray light curve. *Right panel:* Long-term multi-wavelength light curves. Inset shows the zoomed-in late-time optical and X-ray light curves.

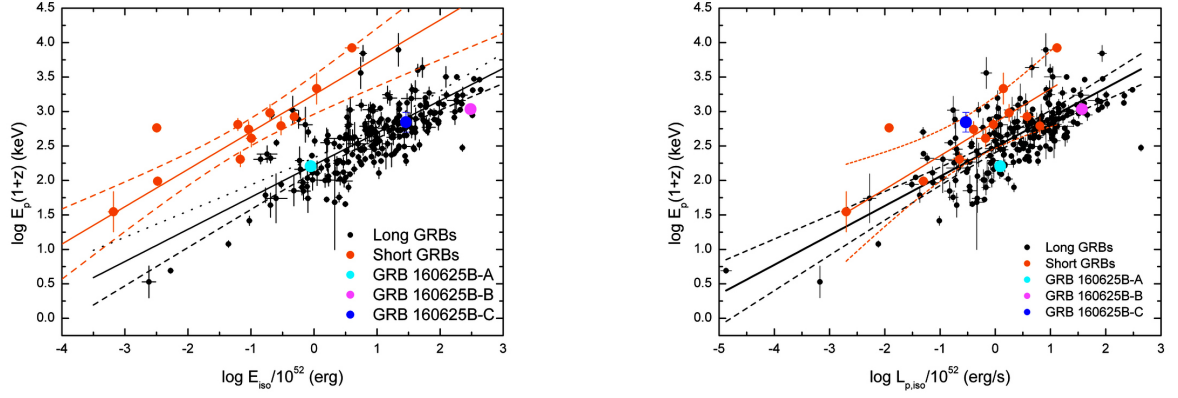


**Figure 3:** The three sub-bursts in GRB 160625B in the  $E_p$ - $E_{\text{iso}}$  and  $E_p$ - $L_{\text{iso}}$  diagrams. All three sub-bursts are consistently located in the typical long (or Type II) GRB regions. The solid lines are the best fit correlations:  $\log E_p/(1+z) = (3.24 \pm 0.07) + (0.54 \pm 0.04)\log(E_{\text{iso}}/10^{52})$  for short GRBs,  $\log E_p/(1+z) = (2.22 \pm 0.03) + (0.47 \pm 0.03)\log(E_{\text{iso}}/10^{52})$  for long GRBs,  $\log E_p/(1+z) = (2.84 \pm 0.09) + (0.49 \pm 0.07)\log(L_{\text{iso}}/10^{52})$  for short GRBs and  $\log E_p/(1+z) = (2.49 \pm 0.03) + (0.43 \pm 0.03)\log(L_{\text{iso}}/10^{52})$  for long GRBs.

## Supplementary Information

### 1. Additional gamma-ray observations of GRB 160625B and localization by the IPN.

GRB 160625B was detected by four InterPlanetary Network (IPN) experiments – *Fermi*-GBM in a low-earth orbit, *INTEGRAL* SPI-ACS[37], in a highly elliptical orbit, *Konus-Wind*[38], in orbit around the Lagrangian point L1, and *Mars-Odyssey* HEND[39], in orbit around Mars – at 0.02, 0.38, 4.32, and 276.46 light-seconds from Earth, respectively. The burst showed three emission episodes: the initial short duration episode (observed by *Konus*, *Fermi*-GBM, SPI-ACS), the main very intense episode (observed by all IPN instruments and *Fermi*-LAT), and the final rather weak episode (observed by GBM, SPI-ACS and *Konus*).

As the two first sub-bursts are entirely different, we cannot exclude that they could be related to two independent events whose wavefronts happened to arrive at Earth 180 s apart. In order to check this we have derived the annuli for the first two sub-bursts (see Fig. S1) and found that both of them are consistent with the Swift-XRT position for GRB 160625B, hence confirming that they very likely have the same origin.

As observed by *Konus*-Wind, the second sub-burst had a fluence of  $9.50 \pm 0.15 \times 10^{-4}$  erg  $\text{cm}^{-2}$ , and a 256-ms peak flux, measured from T0+188.928 s, of  $1.27 \pm 0.07 \times 10^{-4}$  erg  $\text{cm}^{-2}\text{s}^{-1}$  (both in the 20 keV - 10 MeV energy range), which are consistent with *Fermi* observations as listed in Table I.

### 2. Simultaneous Optical Observations of GRB 160625B.

#### 2.1. Very-wide field observation by CASANDRA cameras on the BOOTES Network

Early upper limits were obtained by the CASANDRA all-sky cameras[40] at the BOOTES-1 and BOOTES-2 astronomical stations[41] which were gathering data (as usual) with a 60s time resolution. As the GRB position on the sky was not at optimal conditions, only the above-mentioned upper limits could be derived, although the afterglow is marginally detected at maximum brightness.

#### 2.2. Mini-MegaTORTORA Observation

Mini-MegaTORTORA nine-channel wide-field monitoring system[42] reacted[43] to precursor GBM event and started observing its error box 52 seconds after it and 136 seconds before LAT trigger. Due to large size of GBM error box, the observations have been performed in “widefield+deep” regime, with channels simultaneously covering  $\sim 30 \times 30$  deg field

of view with 30 s exposures in white light to achieve deepest detection limit. The system acquired 20 frames in such regime, covering time interval from  $T_0-136$  to  $T_0+466$  s, and detected a bright optical flash on a frame coincident with LAT trigger time ( $T_0-15.9$  -  $T_0+14.1$  s), with a magnitude of about  $V=8.8$  mag, which then brightened for about 0.1 mag, and then faded following nearly smooth power-law decay with slope of about - 1.6, down to  $V=12.2$  at last acquired frame. The images acquired prior to LAT trigger do not display any object at that position down to about  $V=13.5$  mag. The system also observed the same location between  $T_0+1691$  s and  $T_0+2264$  s, acquiring 20 more 30-s exposure frames. These frames do not display any transient at the position of GRB 160625B brighter than  $V=13.5$  mag.

### 2.3. Pi of the Sky Observation

The Pi of the Sky is a system of wide field of view robotic telescopes, which search for short timescale astrophysical phenomena, especially for prompt optical GRB emission[44]. The system was designed for autonomous operation, monitoring a large fraction of the sky to a depth of  $12^m - 13^m$  and with time resolution of the order of 10 seconds. Custom designed CCD cameras are equipped with Canon lenses  $f=85$  mm,  $f/d = 1.2$  and cover  $20^\circ \times 20^\circ$  of the sky each. The prototype telescope with two cameras is operational in Chile since 2004 (currently at San Pedro de Atacama Observatory) and the final system with 16 cameras on 4 equatorial mounts was completed in 2014 at the INTA El Arenosillo Test Centre in Spain[45].

Cameras of the Pi of the Sky observatory in Spain were not observing the position of the GRB160625B prior to the first sub-burst. Observations started only after receiving Fermi GBM trigger 488587220, about 140 seconds prior to the second sub-burst. As the position estimate taken from Fermi alert and used to position the telescope was not very accurate, the actual position of the burst happened to be in the overlap region of two cameras, CAM35 and CAM39, resulting in two independent sets of measurements. Light curves from both cameras were reconstructed using the LUIZA framework[46, 47]. Observations were performed in wide visible band, with IR-cut and UV-cut filters only, and 10 s exposure time. Images were calibrated to the reference stars from Tycho 2 using the transformation from Tycho to the Pi of the Sky system given by:

$$V_{PI} = V_T + 0.235 - 0.292 \cdot (B_T - V_T)$$



No object brighter than 12.4m ( $3\sigma$  limit) was observed prior to the second sub-burst. An optical flash was identified on an image starting -5.9 s before the time of the LAT trigger, brightening to about 8m on the next image and then becoming gradually dimmer, fading below our sensitivity after about 400 s.

### 3. Additional Optical Observations (photometry)

Additional optical Observations (photometry) The afterglow emission was observed by a dozen of telescopes worldwide: the Zeiss-1000 (1.0m) TSHAO telescope in Kazakhstan, the AS-32 (0.7m) AbAO telescope in Georgia, the AZT-33IK (1.5m) telescope in Mondy (Russia), the AZT-11 (1.25m) and ZTSh (2.6m) telescopes at Crimean Astrophysical Observatory (CrAO), the AZT-22 (1.5m) at Maidanak Observatory (Uzbekistan), the 0.5m MITSuME telescope in Japan, the 1.5m SMARTS telescope at CTIO (Chile), The 6.0m BTA and Zeiss-1000 (1.0m) SAO telescopes at Zelenchuk (Russia), the 1.5m RTT150 telescope in Tübitak (Turkey). and the 0.4m MASTER telescopes worldwide (see Supplementary Table S2 for the detailed optical observations carried out in this work).

**4. Additional optical Observations (spectroscopy)** The 10.4 m Gran Telescopio Canarias (GTC; Canary Island, Spain), equipped with the Optical System for Imaging and Low-Intermediate Resolution Imaging Spectroscopy (OSIRIS) instrument [48] obtained optical spectroscopy at two epochs (2 and 14 days post-burst). Data was reduced and calibrated the usual way using IRAF and custom tools coded up in python. We clearly detect several absorption lines at both epochs, from which a redshift  $z = 1.406 \pm 0.001$  is derived, besides an intervening absorption system at  $z = 1.319$  (see Supplementary Figure S2).

### 5. Additional results

Supplementary Figure S3 shows some typical spectral fit of each sub-burst. Supplementary Figure S5 shows an example fit to the data in one time bin (between 187.23 s and 187.67 s) using the synchrotron model. Supplementary Figure S4 shows an example showing the effect of adding a blackbody component to the Band function model when fitting to the data in the time bin between 187.23 s and 187.67 s. Supplementary Figure S7 shows the correlations between GBM prompt  $\gamma$ -ray (black; 15-350 keV) and optical observations (red) made by Pi of the Sky (Cam 35), Pi of the Sky (Cam 39) and Mini-Mega TORTORA. Supplementary Figure S6 shows the energy-dependent light curves of the three sub-bursts. Supplementary Figure S8 shows the spectral energy distribution (SED) from optical to LAT

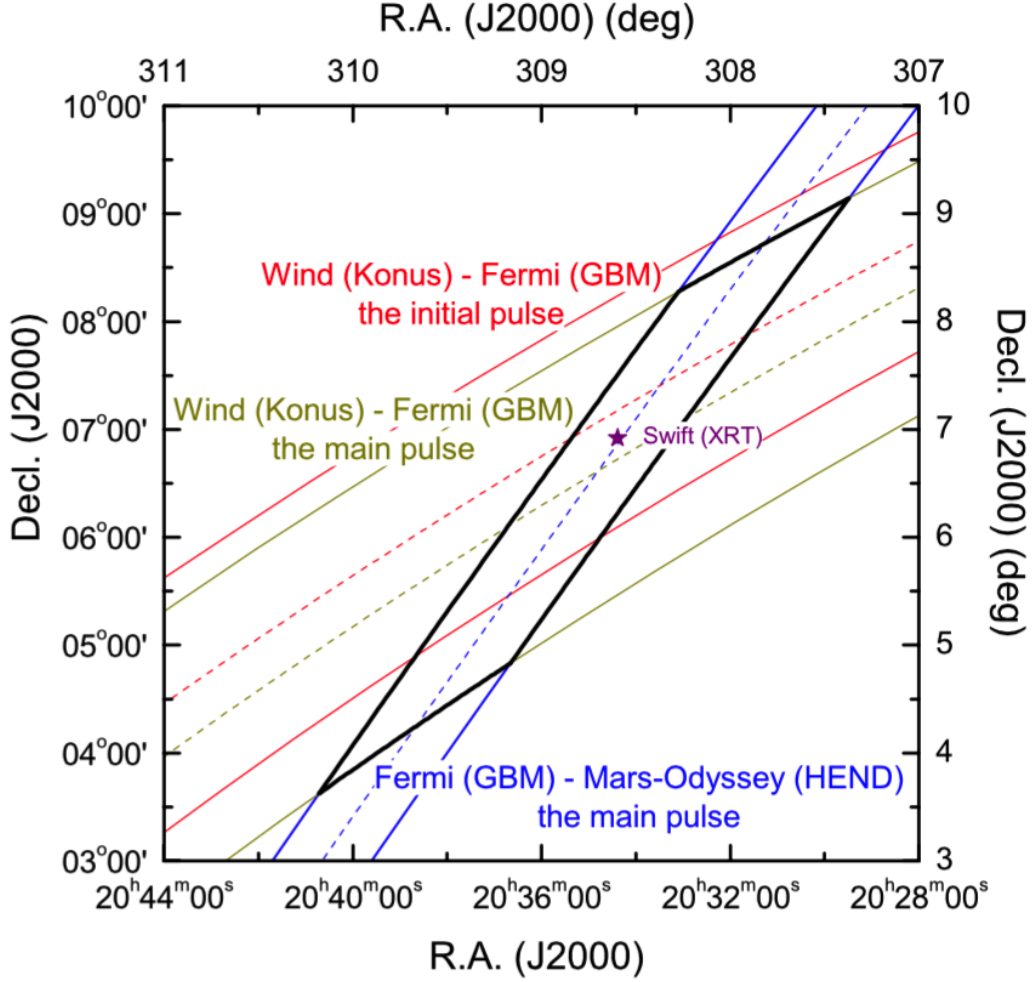


**Figure S1:** The IPN triangulation of first two emission episodes of GRB 160625B. The 1.48 deg wide Wind-Fermi annulus derived for the first episode (1st sub-burst, 0.84 s duration) is consistent with *Swift*-XRT position (indicated by the star) and the IPN error box defined by *Wind-Fermi* and *Fermi-Mars-Odyssey* annuli derived for the main episode (2nd sub-burst).

energies in each optical observational bins during the second sub-burst. Supplementary Table S1 shows the time-resolved spectral fitting results. Supplementary Table S2 shows the optical observations of GRB 160625B. Supplementary Table S3 shows the best-fit parameters of the synchrotron model fitted to the spectra between 187.23 s and 187.67 s. Supplementary Table S4 shows time lag of optical light curves with respect to the  $\gamma$ -ray light curve in the 2nd sub-burst. Supplementary Table S5 shows Spectral fitting parameters for the three SED slices.

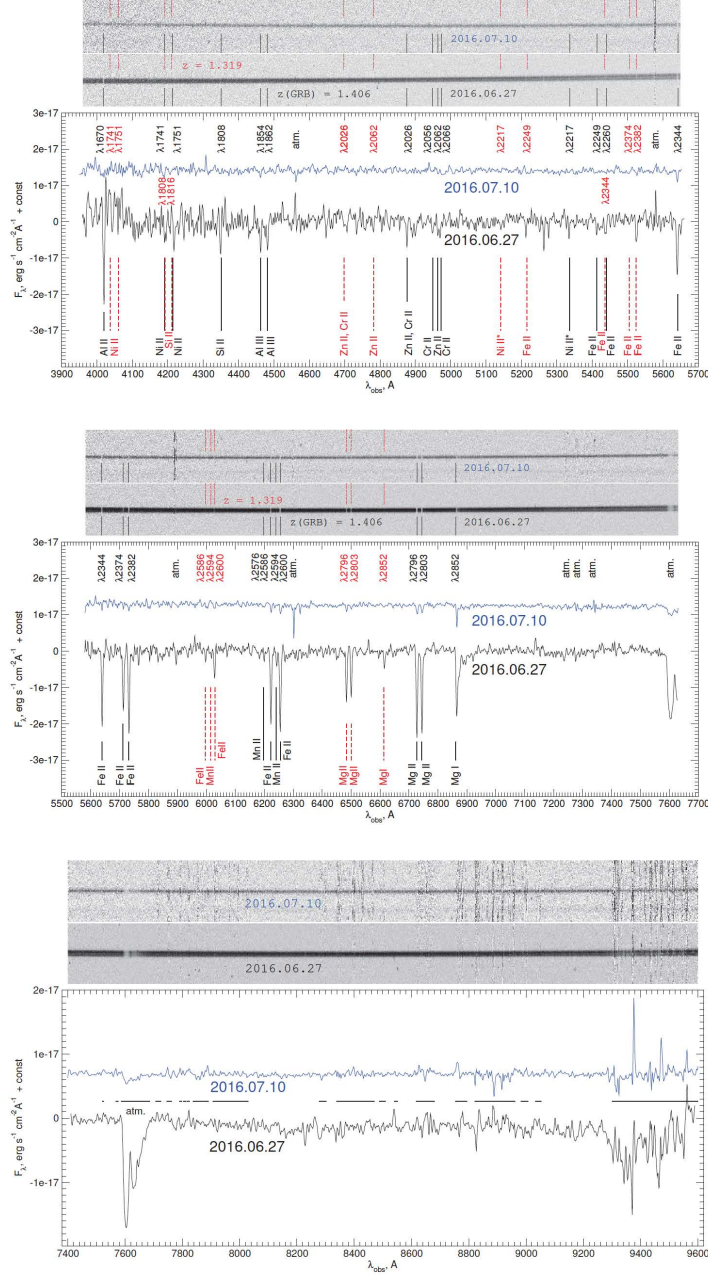


**Figure S2:** Spectra of GRB 160625B were obtained with the 10.4m GTC telescope (Osiris) on 2016.06.27 (bottom, black line) and 2016.07.10 (top, blue line). Absorption lines at  $z(\text{GRB}) = 1.406$  is marked by solid black lines. An intervening absorption system at  $z = 1.319$  is marked by red dashed lines. Spectra was shootted with the Gaussian core (2.8 Å, 4.4 Å and 3.2 Å for the blue, red and infrared parts respectively). Among the numerous atmospheric lines in the infrared part of spectra (marked by the horizontal bands) we do not detect the [OII] lines at both the GRB redshift or the intervening system. See also [51]

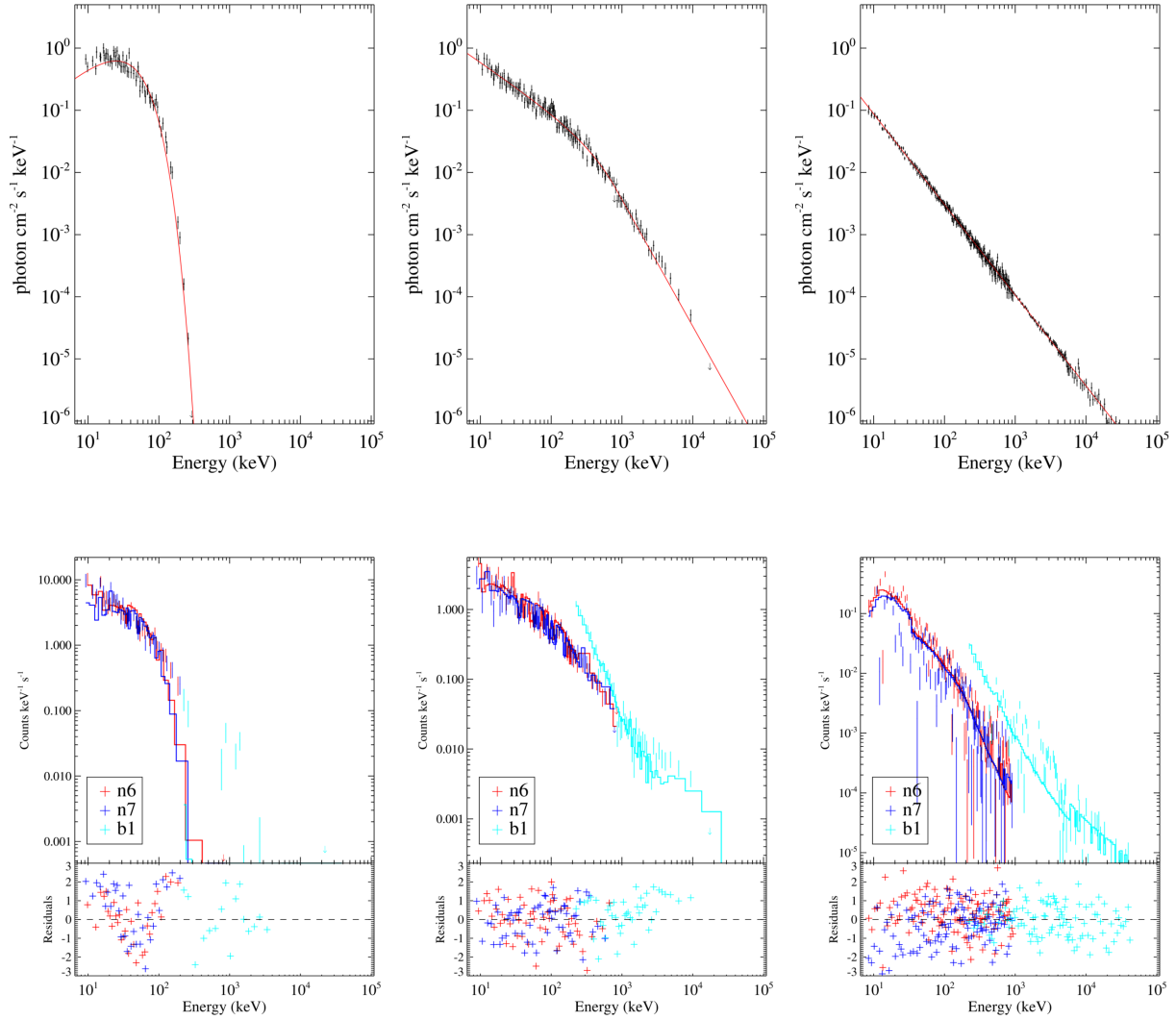


**Figure S3:** Typical spectral fit of each sub-burst. From left to right: black body fit of the 1st sub-burst between 0.13 and 0.35 s, Band function fit of the 2nd sub-burst between 187.23 and 187.67 s and power law fit of the 3rd sub-burst between 520.00 and 535.00 s. Top: photon spectra. Note the instrumental response has been deconvolved in each plot of the photon spectra. Bottom: Observed count rate spectra. The best-fit parameters can be found in Table S1.

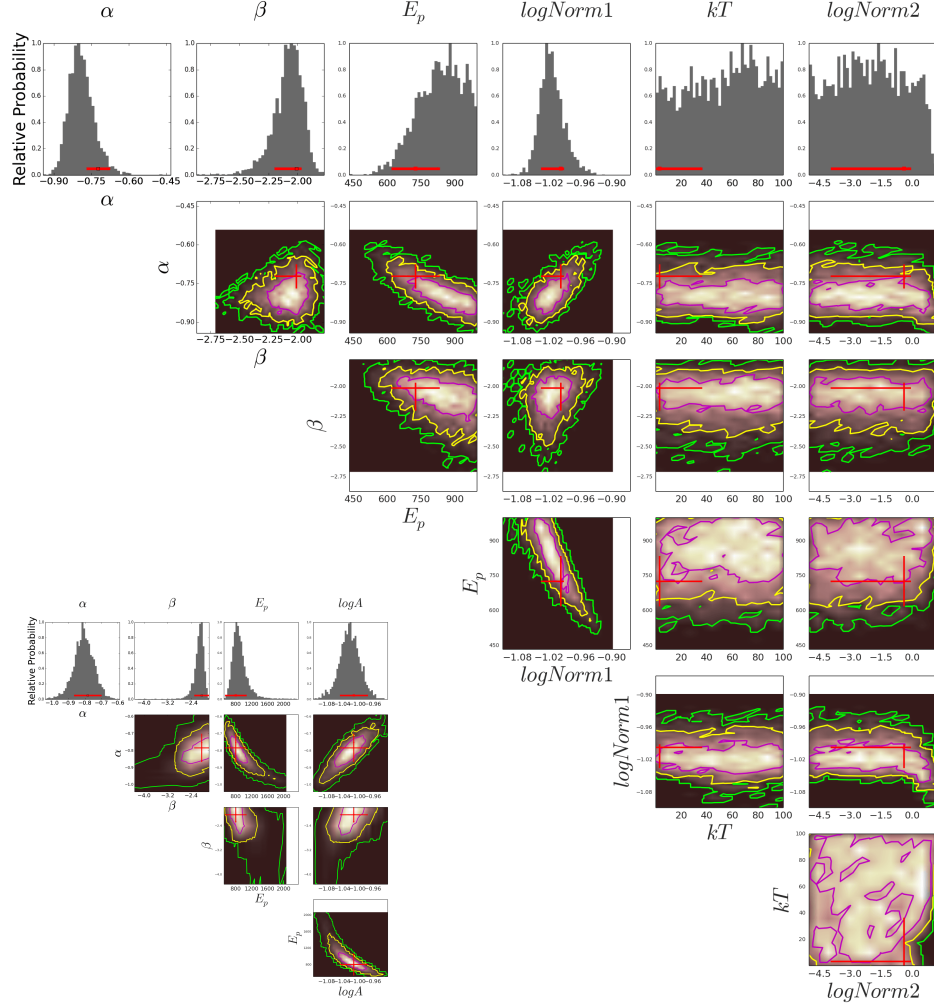


**Figure S4:** An example showing the effect of adding a blackbody component to the Band function model when fitting to the data in the time bin between 187.23 s and 187.67 s. *Bottom Left:* the likelihood map of the parameter-constraint outputs for the Band fit, where all the parameters are constrained. The goodness of fit, PGSTAT/dof, as shown in Supplementary Table S1, is 335.55/360. *Upper Right:* the likelihood map of the parameter-constraint outputs for the Band+blackbody fit. The PGSTAT/dof is 334.01/358. According to the Bayesian information criterion (BIC[49]), such value of goodness does not imply any improvement in comparison with the Band-only fit. More importantly, we noticed the flat-shape of likelihood map of the two blackbody parameters (i.e, blackbody temperate  $kT$  and normalization parameter  $\log\text{Norm2}$ ), implying they are unconstrained. The fluence of the such blackbody component is only  $\sim 0.05\%$  of the total fluence. Above facts suggest that the blackbody component is not required to fit the observational data.

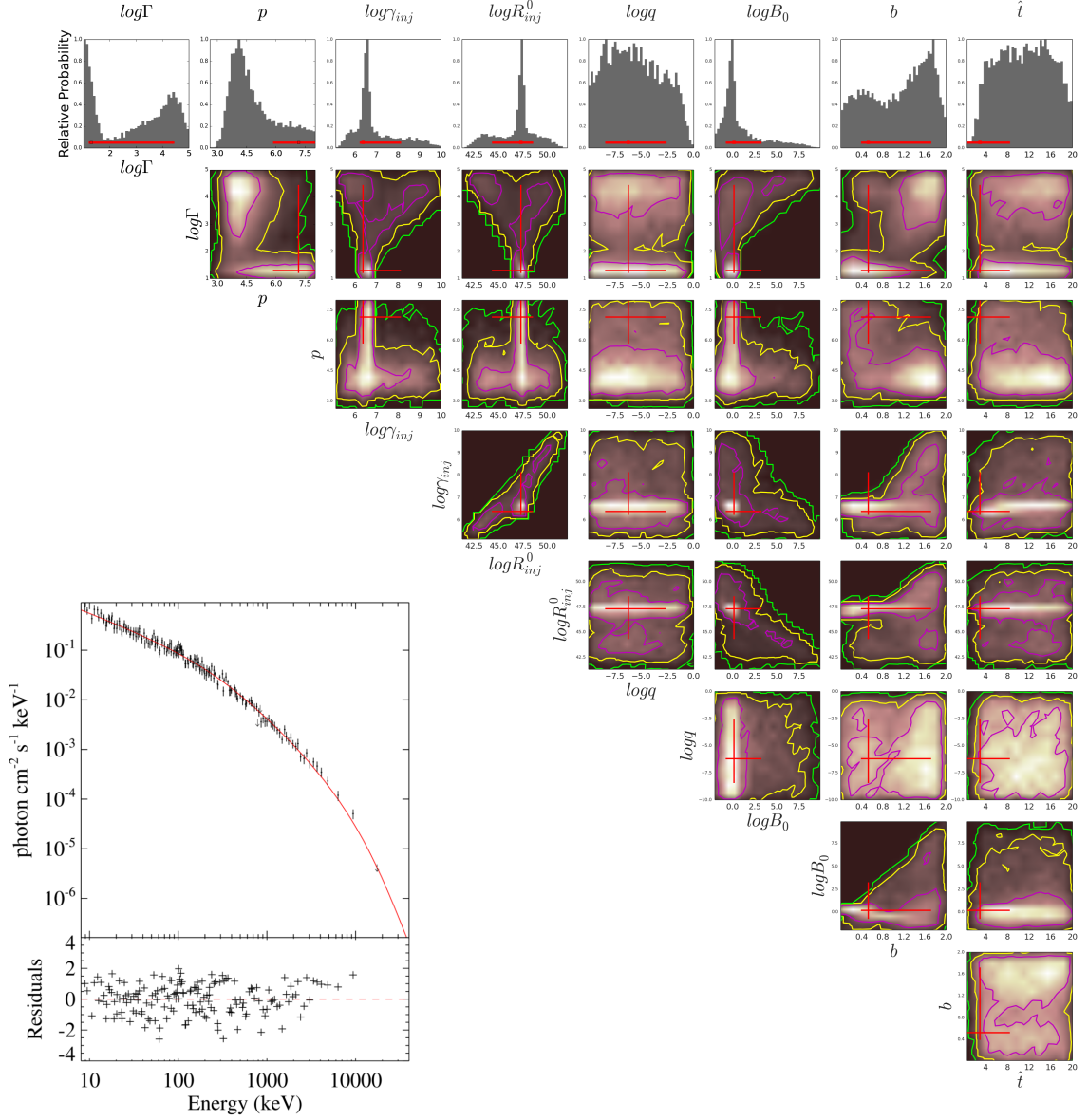


**Figure S5:** An example fit to the data in one time bin (between 187.23 s and 187.67 s) using the synchrotron model (bottom-left) and constraints on the model parameters (upper-right). Histograms and contours show the likelihood map of the parameter-constraint outputs from our McSpecFit package. Red crosses mark the best-fit values and  $1\sigma$  error bars. All the constrained parameters fall into the reasonable ranges for the synchrotron theoretical model. A Band function can equally fit to the data with  $\alpha=-0.8$  and  $\beta=-2.0$  (Table S1).

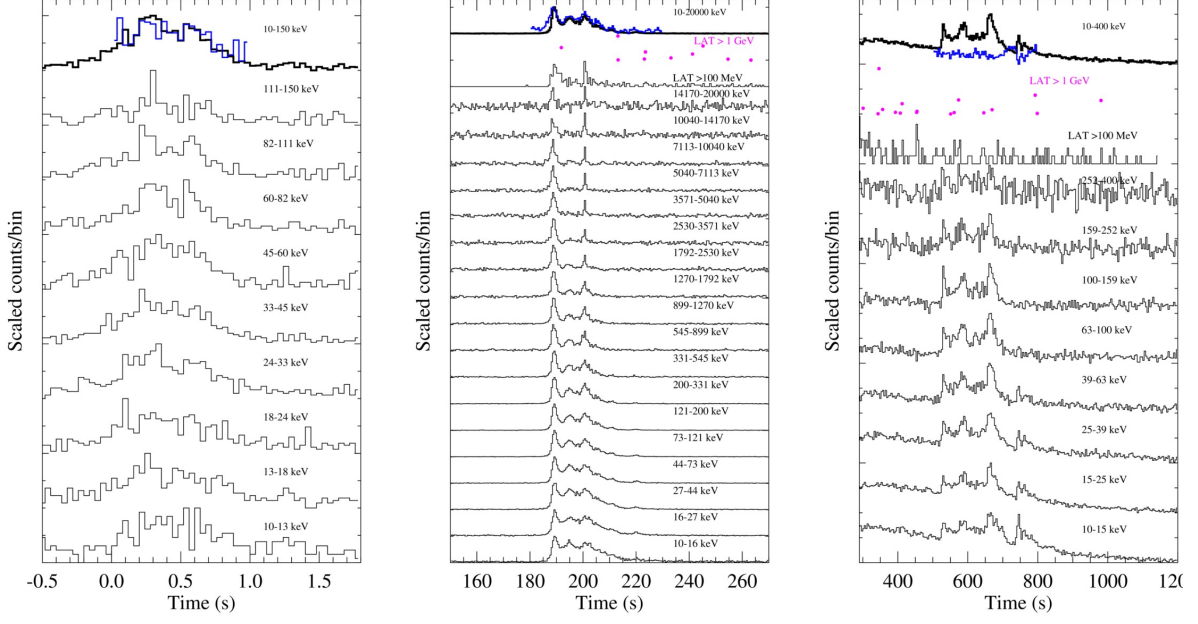


**Figure S6:** Energy-dependent light curves of the three sub-bursts. In each plot, the lightcurves in each energy bin are plotted in lower panels, and the full-energy-range light curves are plotted in the top panel with the thick black curves. Also the hardness ratios (defined as  $HR = \frac{Rate_{E_2, E_3}}{Rate_{E_1, E_2}}$ , where  $E_1$  and  $E_3$  define the lower and higher end of the energy range of the selected NaI detectors, and  $E_2 = \sqrt{E_1 \times E_3}$ ) are plotted in solid blue curves. The LAT-band photons are plotted individually for the 2nd and 3rd sub-bursts.

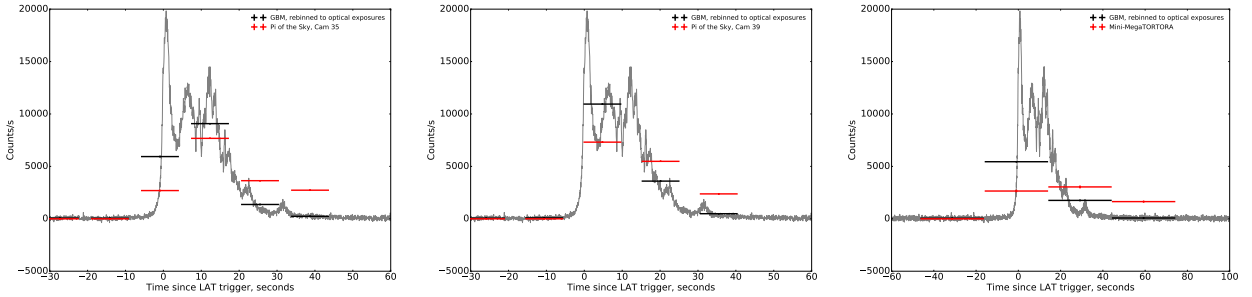


**Figure S7:** Correlations between GBM prompt  $\gamma$ -ray (black; 15-350 keV) and optical observations (red) made by Pi of the Sky (Cam 35), Pi of the Sky (Cam 39) and Mini-Mega TORTORA respectively. Lags are calculated between the optical flux and the averaged GBM count rate in the optical exposure intervals. The values of lag are listed in Table S4.



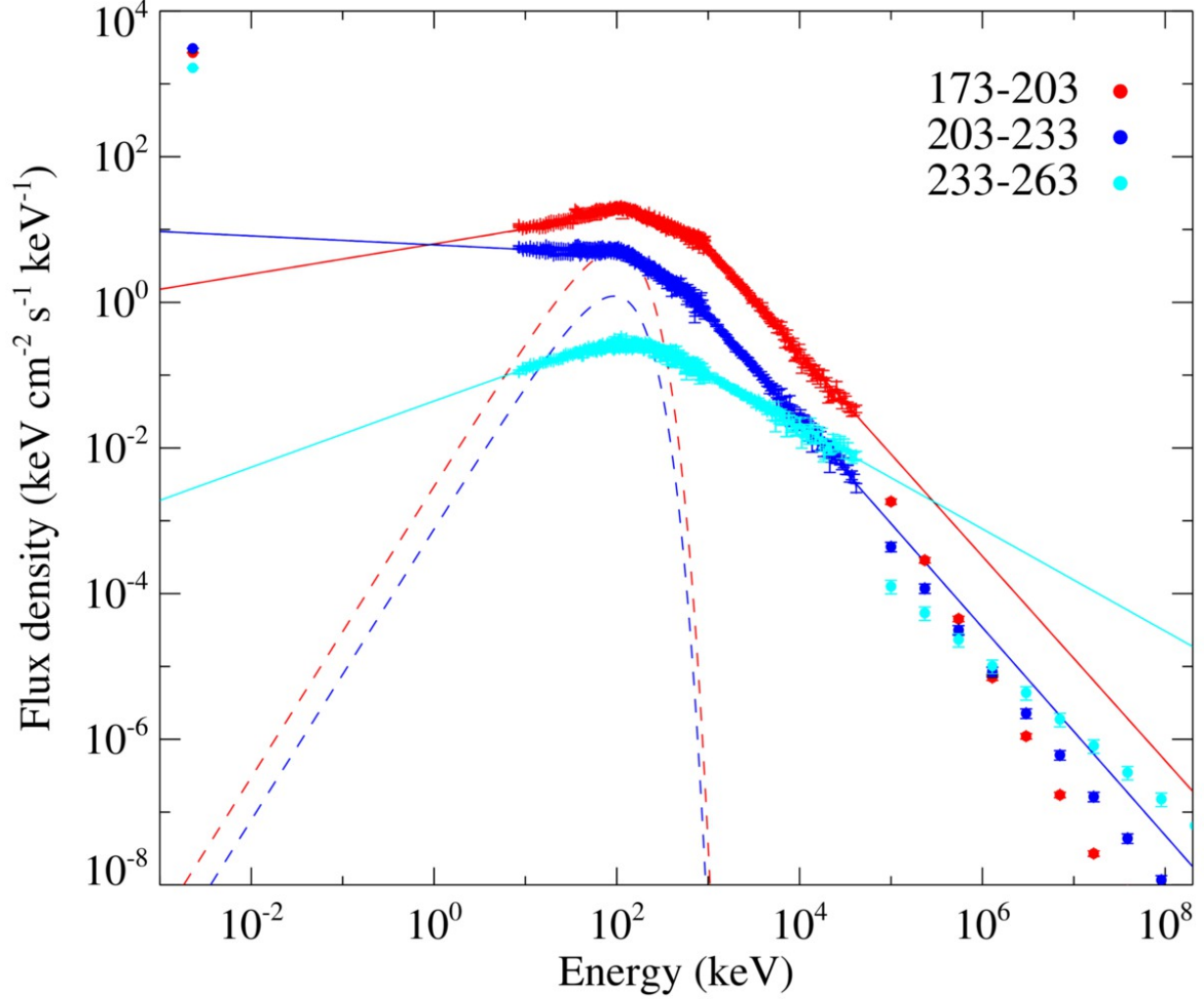


**Figure S8:** The spectral energy distribution (SED) from optical to LAT energies in each optical observational bins during the second sub-burst. The model curves (solid lines) are derived using GBM data only, which are extrapolated to the optical and LAT energy bands. Such model curves are only rough estimates of the true SEDs due to the large time bins used and the goodness of those fits is not statistically favorable (Table S5). Adding an additional blackbody component (dashed) significantly improves the goodness of the fits from the Band-only case (Table S5). However, such an apparent blackbody component is an effect of spectral evolution, since in finer spectral bins, no blackbody component is needed (Figure 1 and Table S1).



TABLE S1: Time-resolved Spectral fitting

$(t_1, t_2)$	kT (keV)	$r_0 \times Y^{3/2}$ (cm)	$\Gamma \times Y^{-1/4}$	PGSTAT/dof
(-0.30,-0.08)	$9.06^{+2.33}_{-1.24}$	$4.6 \times 10^8$	214	203.42/362
(-0.08,0.13)	$13.64^{+0.63}_{-0.67}$	$4.6 \times 10^8$	323	222.68/362
(0.13,0.35)	$15.59^{+0.50}_{-0.46}$	$5.2 \times 10^8$	381	278.12/362
(0.35,0.57)	$15.38^{+0.51}_{-0.45}$	$4.9 \times 10^8$	370	228.15/362
(0.57,0.78)	$14.60^{+0.57}_{-0.54}$	$4.7 \times 10^8$	348	209.76/362
(0.78,1.00)	$8.47^{+1.08}_{-0.77}$	$7.2 \times 10^8$	224	217.85/362
$(t_1, t_2)$	$\alpha$	$\beta$	$E_p$ (keV)	PGSTAT/dof
(187.23,187.67)	$-0.78^{+0.04}_{-0.08}$	$-2.04^{+0.05}_{-0.25}$	$806.38^{+271.15}_{-61.44}$	335.55/360
(187.67,188.04)	$-0.70^{+0.04}_{-0.06}$	$-1.98^{+0.06}_{-0.10}$	$757.66^{+140.77}_{-73.09}$	385.54/360
(188.04,188.16)	$-0.73^{+0.03}_{-0.11}$	$-2.10^{+0.07}_{-0.52}$	$912.39^{+441.55}_{-79.77}$	337.65/360
(188.16,188.33)	$-0.72^{+0.04}_{-0.05}$	$-2.18^{+0.08}_{-0.18}$	$995.84^{+177.44}_{-94.27}$	383.20/360
(188.33,188.56)	$-0.61^{+0.03}_{-0.03}$	$-2.11^{+0.05}_{-0.06}$	$797.45^{+59.23}_{-57.06}$	470.96/360
(188.56,188.76)	$-0.62^{+0.03}_{-0.03}$	$-2.14^{+0.05}_{-0.07}$	$794.14^{+62.27}_{-52.33}$	385.24/360
(188.76,188.96)	$-0.63^{+0.03}_{-0.03}$	$-2.13^{+0.05}_{-0.07}$	$711.24^{+57.30}_{-47.08}$	396.40/360
(188.96,189.06)	$-0.63^{+0.05}_{-0.05}$	$-2.19^{+0.08}_{-0.13}$	$691.62^{+81.39}_{-75.76}$	448.78/360
(189.06,189.16)	$-0.60^{+0.04}_{-0.06}$	$-2.23^{+0.08}_{-0.11}$	$611.75^{+75.05}_{-41.58}$	423.54/360
(189.16,189.37)	$-0.59^{+0.02}_{-0.04}$	$-2.22^{+0.05}_{-0.08}$	$595.18^{+50.44}_{-29.04}$	395.99/360
(189.37,189.48)	$-0.62^{+0.05}_{-0.04}$	$-2.18^{+0.09}_{-0.08}$	$611.49^{+54.98}_{-59.86}$	393.04/360
(189.47,189.58)	$-0.58^{+0.04}_{-0.05}$	$-2.18^{+0.06}_{-0.11}$	$519.47^{+61.29}_{-34.26}$	410.86/360
(189.58,189.78)	$-0.56^{+0.04}_{-0.03}$	$-2.17^{+0.06}_{-0.06}$	$495.36^{+30.30}_{-31.37}$	400.01/360
(189.78,189.98)	$-0.61^{+0.03}_{-0.05}$	$-2.17^{+0.07}_{-0.08}$	$514.59^{+52.29}_{-30.36}$	396.81/360
(189.98,190.04)	$-0.62^{+0.09}_{-0.08}$	$-2.17^{+0.13}_{-0.15}$	$403.14^{+71.68}_{-53.70}$	290.77/360
(190.04,190.33)	$-0.65^{+0.04}_{-0.03}$	$-2.14^{+0.06}_{-0.07}$	$475.64^{+37.32}_{-32.42}$	407.86/360
(190.33,190.96)	$-0.66^{+0.03}_{-0.03}$	$-2.18^{+0.04}_{-0.07}$	$402.28^{+23.41}_{-22.83}$	471.62/360
(190.96,191.47)	$-0.63^{+0.04}_{-0.05}$	$-2.20^{+0.05}_{-0.10}$	$327.40^{+29.13}_{-18.13}$	365.25/360
(191.47,192.47)	$-0.66^{+0.02}_{-0.04}$	$-2.27^{+0.04}_{-0.07}$	$295.09^{+16.74}_{-10.80}$	450.68/360
(192.47,192.85)	$-0.71^{+0.04}_{-0.04}$	$-2.54^{+0.37}_{-6.46}$	$334.05^{+29.25}_{-29.25}$	326.52/360
(192.85,193.19)	$-0.60^{+0.05}_{-0.05}$	$-2.35^{+0.09}_{-0.12}$	$299.31^{+23.84}_{-19.88}$	384.56/360
(193.19,194.14)	$-0.64^{+0.02}_{-0.02}$	$-2.44^{+0.05}_{-0.09}$	$416.01^{+17.06}_{-12.83}$	477.81/360
(194.14,194.46)	$-0.68^{+0.03}_{-0.04}$	$-2.75^{+0.13}_{-0.63}$	$469.09^{+40.35}_{-19.46}$	409.00/360
(194.46,194.76)	$-0.68^{+0.02}_{-0.04}$	$-2.79^{+0.13}_{-0.47}$	$527.72^{+42.41}_{-19.19}$	455.57/360
(194.74,195.36)	$-0.63^{+0.02}_{-0.03}$	$-2.49^{+0.07}_{-0.08}$	$430.53^{+20.55}_{-12.95}$	435.11/360
(195.14,195.66)	$-0.60^{+0.03}_{-0.03}$	$-2.37^{+0.07}_{-0.08}$	$389.85^{+20.85}_{-18.75}$	427.55/360
(195.66,196.16)	$-0.64^{+0.02}_{-0.04}$	$-2.54^{+0.07}_{-0.25}$	$420.02^{+36.58}_{-12.69}$	440.93/360
(196.16,196.42)	$-0.66^{+0.04}_{-0.06}$	$-2.39^{+0.09}_{-0.27}$	$406.81^{+46.99}_{-27.44}$	372.77/360
(196.46,196.82)	$-0.67^{+0.03}_{-0.03}$	$-2.79^{+0.46}_{-6.66}$	$408.09^{+22.14}_{-22.14}$	404.01/360
(196.82,197.51)	$-0.73^{+0.03}_{-0.04}$	$-2.41^{+0.08}_{-0.16}$	$405.62^{+28.31}_{-23.65}$	459.31/360
(197.51,198.07)	$-0.73^{+0.01}_{-0.04}$	$-3.12^{+0.59}_{-6.15}$	$534.16^{+21.26}_{-21.26}$	436.09/360
(198.07,198.47)	$-0.71^{+0.03}_{-0.04}$	$-2.45^{+0.09}_{-0.20}$	$425.78^{+38.86}_{-20.96}$	366.34/360
(198.47,198.83)	$-0.80^{+0.03}_{-0.04}$	$-3.66^{+1.09}_{-6.03}$	$471.09^{+44.33}_{-12.77}$	353.59/360
(198.83,199.46)	$-0.74^{+0.01}_{-0.03}$	$-3.19^{+0.63}_{-6.67}$	$500.14^{+33.15}_{-3.56}$	399.37/360
(199.46,199.89)	$-0.66^{+0.02}_{-0.03}$	$-2.77^{+0.12}_{-0.32}$	$580.51^{+32.85}_{-24.63}$	389.78/360
(199.89,200.29)	$-0.68^{+0.02}_{-0.04}$	$-2.78^{+0.09}_{-0.39}$	$604.95^{+50.79}_{-15.58}$	408.52/360
(200.29,200.48)	$-0.74^{+0.03}_{-0.06}$	$-2.23^{+0.09}_{-0.20}$	$652.73^{+107.08}_{-51.17}$	454.37/360
(200.48,200.68)	$-0.68^{+0.04}_{-0.04}$	$-1.94^{+0.04}_{-0.07}$	$650.16^{+85.37}_{-50.93}$	436.57/360
(200.68,200.98)	$-0.63^{+0.03}_{-0.03}$	$-2.13^{+0.06}_{-0.05}$	$600.54^{+37.90}_{-36.03}$	434.81/360
(200.98,201.23)	$-0.70^{+0.02}_{-0.04}$	$-2.50^{+0.07}_{-0.22}$	$601.52^{+50.43}_{-27.57}$	346.01/360
(201.23,201.54)	$-0.51^{+0.04}_{-0.07}$	$-2.27^{+0.07}_{-0.11}$	$348.36^{+35.20}_{-18.36}$	353.90/360
(201.54,201.83)	$-0.77^{+0.01}_{-0.04}$	$-3.30^{+0.77}_{-5.91}$	$537.52^{+46.32}_{-7.59}$	427.30/360
(201.83,202.10)	$-0.68^{+0.01}_{-0.04}$	$-3.04^{+0.51}_{-6.45}$	$554.86^{+48.08}_{-3.19}$	437.78/360
(202.10,202.38)	$-0.68^{+0.03}_{-0.03}$	$-2.92^{+0.46}_{-6.32}$	$554.26^{+35.02}_{-35.02}$	413.80/360
(202.38,202.68)	$-0.80^{+0.02}_{-0.04}$	$-3.89^{+1.26}_{-5.76}$	$455.98^{+32.04}_{-13.44}$	400.63/360
(202.68,203.03)	$-0.78^{+0.01}_{-0.05}$	$-2.79^{+0.42}_{-6.25}$	$478.94^{+59.03}_{-6.50}$	411.35/360
(203.03,203.61)	$-0.79^{+0.02}_{-0.03}$	$-3.18^{+0.61}_{-6.48}$	$466.08^{+30.27}_{-12.21}$	426.47/360
(203.61,204.21)	$-0.89^{+0.01}_{-0.04}$	$-3.14^{+0.75}_{-6.33}$	$461.94^{+41.47}_{-11.18}$	389.57/360
(204.21,205.21)	$-0.81^{+0.02}_{-0.04}$	$-2.62^{+0.10}_{-0.51}$	$441.88^{+39.46}_{-17.18}$	431.78/360
(205.21,206.18)	$-0.76^{+0.02}_{-0.05}$	$-2.63^{+0.04}_{-6.57}$	$401.49^{+45.70}_{-10.23}$	450.97/360
(206.18,206.78)	$-0.69^{+0.02}_{-0.08}$	$-2.76^{+0.03}_{-11.86}$	$260.54^{+31.03}_{-2.98}$	429.98/360
(206.78,207.78)	$-0.75^{+0.03}_{-0.06}$	$-2.34^{+0.09}_{-0.21}$	$259.57^{+27.57}_{-12.05}$	433.37/360

TABLE S1: Time-resolved Spectral fitting (continued)

$(t_1, t_2)$	$\alpha$	$\beta$	$E_p$ (keV)	PGSTAT/dof
(207.78,208.37)	$-0.76^{+0.04}_{-0.12}$	$-2.32^{+0.07}_{-2.61}$	$214.76^{+49.99}_{-9.72}$	394.46/360
(208.37,208.97)	$-0.90^{+0.05}_{-0.06}$	$-3.00^{+0.58}_{-6.09}$	$232.88^{+29.37}_{-6.50}$	387.05/360
(208.97,210.47)	$-0.84^{+0.04}_{-0.04}$	$-2.43^{+0.31}_{-6.66}$	$238.76^{+19.08}_{-19.08}$	376.16/360
(210.47,211.81)	$-0.87^{+0.05}_{-0.05}$	$-2.38^{+0.31}_{-6.93}$	$264.60^{+25.86}_{-25.86}$	420.99/360
(211.81,214.97)	$-1.08^{+0.01}_{-0.12}$	$-2.15^{+0.27}_{-6.82}$	$183.20^{+32.55}_{-32.55}$	404.11/360
(214.97,215.47)	$-1.15^{+0.11}_{-0.26}$	$-12.74^{+7.59}_{-4.68}$	$263.12^{+568.59}_{-36.64}$	281.61/360
(215.47,218.24)	$-1.17^{+0.09}_{-0.09}$	$-1.96^{+0.26}_{-7.04}$	$223.68^{+101.53}_{-82.42}$	363.91/360
(520.00,535.00)	$-1.39^{+0.02}_{-0.03}$			349.13/362
(535.00,542.00)	$-1.51^{+0.04}_{-0.06}$			320.62/362
(542.00,559.00)	$-1.52^{+0.03}_{-0.05}$			403.90/362
(570.00,578.00)	$-1.08^{+0.03}_{-0.04}$			366.79/362
(578.00,585.00)	$-1.54^{+0.03}_{-0.03}$			425.14/362
(585.00,593.00)	$-1.20^{+0.07}_{-0.13}$		$188.61^{+70.23}_{-19.34}$	384.23/361
(593.00,600.00)	$-1.33^{+0.05}_{-0.05}$			413.41/362
(650.00,658.00)	$-1.59^{+0.03}_{-0.04}$			353.24/362
(658.00,661.50)	$-1.40^{+0.06}_{-0.21}$		$171.80^{+262.90}_{-16.82}$	411.65/361
(661.50,665.00)	$-1.47^{+0.02}_{-0.03}$			411.45/362
(665.00,669.00)	$-1.30^{+0.03}_{-0.03}$			437.81/362
(669.00,673.00)	$-1.44^{+0.03}_{-0.04}$			386.22/362
(673.00,680.00)	$-1.68^{+0.03}_{-0.04}$			399.92/362
(740.00,750.00)	$-2.31^{+0.07}_{-0.08}$			397.40/362
(750.00,760.00)	$-2.76^{+0.19}_{-0.29}$			318.07/362
(760.00,770.00)	$-2.37^{+0.12}_{-0.13}$			379.96/362
(770.00,780.00)	$-2.49^{+0.25}_{-0.33}$			319.50/362

TABLE S2: Optical observations of GRB 160625B.

$T_{\text{mid}}(\text{s})$	$T_{\text{exp}}(\text{s})$	Mag	Error	Band	$T_{\text{mid}}(\text{s})$	$T_{\text{exp}}(\text{s})$	Mag	Error	Band
BOOTES-1 and BOOTES-2									
-27.28	36	>7.5		R	41.72	> 36	>7.5		R
Mini-MegaTORTORA									
187.90	30	8.67	0.004	V	429.30	30	11.16	0.02	V
218.00	30	8.52	0.004	V	459.40	30	11.28	0.02	V
248.10	30	9.19	0.01	V	489.50	30	11.50	0.03	V
278.20	30	9.53	0.01	V	519.60	30	11.63	0.03	V
308.60	30	9.91	0.01	V	550.00	30	11.78	0.03	V
338.70	30	10.24	0.01	V	580.10	30	11.87	0.04	V
368.80	30	10.56	0.01	V	610.20	30	11.98	0.04	V
398.90	30	10.85	0.02	V	640.30	30	12.14	0.05	V
67.20	30	>13.85		V	2136.60	30	>13.82		V
97.30	30	>13.76		V	2166.69	30	>13.68		V
127.40	30	>13.75		V	2196.79	30	>13.78		V
157.50	30	>13.9		V	2226.89	30	>13.83		V
1895.19	30	>13.79		V	2257.30	30	>13.8		V
1925.29	30	>13.74		V	2287.39	30	>13.84		V
1955.39	30	>13.7		V	2317.40	30	>13.79		V
1985.49	30	>13.79		V	2347.49	30	>13.82		V
2015.89	30	>13.67		V	2377.89	30	>13.7		V
2045.99	30	>13.71		V	2407.90	30	>13.66		V
2076.09	30	>13.8		V	2437.99	30	>13.7		V
2106.19	30	>13.76		V	2468.09	30	>13.73		V
Pi of the Sky 35									
187.10	10	9.18	0.02	V	369.79	10	11.11	0.12	V
200.30	10	8.04	0.01	V	383.00	10	11.28	0.14	V

*Continued on next page*

– Continued from previous page

$T_{mid}(s)$	$T_{exp}(s)$	Mag	Error	Band	$T_{mid}(s)$	$T_{exp}(s)$	Mag	Error	Band
213.50	10	8.85	0.01	V	396.20	10	11.43	0.16	V
226.71	10	9.16	0.02	V	409.41	10	11.52	0.17	V
239.91	10	9.35	0.02	V	422.60	10	11.66	0.20	V
253.13	10	9.48	0.03	V	435.80	10	11.97	0.26	V
266.33	10	9.76	0.03	V	448.99	10	11.44	0.16	V
279.53	10	9.89	0.04	V	462.19	10	12.23	0.33	V
303.76	10	10.36	0.06	V	475.39	10	11.71	0.20	V
316.97	10	10.36	0.06	V	488.60	10	12.10	0.30	V
330.17	10	10.66	0.08	V	501.80	10	12.02	0.27	V
343.38	10	10.78	0.09	V	541.41	10	12.15	0.30	V
356.58	10	10.90	0.10	V	581.02	10	12.21	0.33	V
Pi of the Sky 39									
192.78	10	8.08	0.01	V	362.12	10	10.99	0.12	V
208.13	10	8.40	0.01	V	377.47	10	11.23	0.15	V
223.48	10	9.30	0.03	V	392.82	10	11.05	0.13	V
238.83	10	9.38	0.03	V	408.17	10	11.27	0.16	V
254.69	10	9.60	0.03	V	425.57	10	11.47	0.19	V
270.04	10	9.76	0.04	V	440.89	10	12.00	0.31	V
285.39	10	10.00	0.05	V	456.75	10	11.79	0.25	V
300.72	10	10.24	0.06	V	472.10	10	12.09	0.34	V
316.07	10	10.44	0.07	V	487.45	10	11.95	0.30	V
331.42	10	10.64	0.09	V	518.15	10	12.14	0.35	V
346.77	10	10.79	0.10	V	625.60	10	12.19	0.37	V
TSHAO									
79301.38	6960	18.90	0.05	R	2405985.98	6600	>21.7		R
247220.64	7560	20.32	0.06	R	2491992.00	6600	>22.0		R
764124.19	2400	21.33	0.18	R	3182164.70	3120	>21.9		R

Continued on next page

– *Continued from previous page*

$T_{mid}(s)$	$T_{exp}(s)$	Mag	Error	Band	$T_{mid}(s)$	$T_{exp}(s)$	Mag	Error	Band
1029271.10	2160	21.67	0.29	R	3273906.82	10080	>22.7		R
1116053.86	11700	21.61	0.16	R	3354166.37	5040	>22.5		R
1284887.23	8700	21.64	0.09	R	3268571.62	18240	>23.0		R
1378602.72	5100	21.89	0.34	R	3785611.68	2760	>22.0		R
1464446.30	5700	21.92	0.28	R	3964933.15	1560	>21.1		R
AbAO									
166746.82	3240	19.61	0.06	CR	1731695.33	4020	22.13	0.21	CR
424964.45	1380	20.75	0.37	CR	1896639.84	3000	>21.7		CR
518178.82	1980	20.89	0.17	CR	2594973.89	3840	22.24	0.26	CR
693245.09	1620	21.22	0.18	CR	2682638.78	3840	>22.5		CR
1559670.34	2880	21.87	0.35	CR	3026274.05	4800	>22.9		CR
Mondy									
328701.02	3600	20.33	0.10	R	1360882.94	3600	21.93	0.11	R
757106.78	3480	21.13	0.09	R	2394252.00	4500	>21.6		R
CrAO									
84461.18	3240	18.87	0.10	R	2935651.68	3600	23.05	0.08	R
2680685.28	4080	22.88	0.09	R	5730540.48	3840	>23.8		R
2847137.47	5760	23.10	0.07	R					
Maidanak									
1122346.37	1800	21.75	0.11	R	1891335.74	5400	22.30	0.34	R
1208215.01	1800	21.55	0.08	R	2326797.79	4320	22.45	0.26	R
1294950.24	1800	21.71	0.09	R	3480784.70	3600	23.31	0.10	R
1373255.42	1800	21.97	0.11	R	3830392.80	13800	23.69	0.11	R
1462217.18	1800	22.02	0.10	R	4608813.6	8400	>22.8		R
1552235.62	1800	22.12	0.17	R					
SAO RAS									
170726.40	2100	19.87	0.07	R	348710.40	2400	20.56	0.20	R

*Continued on next page*

TABLE S3: Best-Fit Parameters of the Synchrotron Model Fitted to the Spectra Between 187.23 s and 187.67 s

Parameter Name	Value	error(-)	error (+)
$\log\Gamma$	1.29	0.09	3.15
p	7.16	1.30	0.84
$\log\gamma_{inj}$	6.38	0.16	1.75
$\log R_{inj}^0$	47.31	2.98	1.24
$\log q$	-6.20	2.24	3.61
$\log B_0$	0.188	0.95	3.08
b	0.53	0.14	1.19
$\hat{t}$	2.95	2.36	5.52

TABLE S4: Time lag of optical light curves with respect to the  $\gamma$ -ray light curve in the 2nd sub-burst

Band	lag (s)
Pi 35 vs GBM	$3.1^{+1.4}_{-2.1}$
Pi 39 vs GBM	$3.3^{+1.3}_{-1.1}$
Mini-MegaTORTORA vs GBM	$4.8^{+5.1}_{-4.7}$

– *Continued from previous page*

$T_{mid}(s)$	$T_{exp}(s)$	Mag	Error	Band	$T_{mid}(s)$	$T_{exp}(s)$	Mag	Error	Band
335232.00	600	20.53	0.07	R	3276451.30	720	23.47	0.10	R

TABLE S5: Spectral fitting parameters for the three SED slices

$(t_1, t_2)$	kT (keV)	$\alpha$	$\beta$	$E_p$ (keV)	PGSTAT/dof
(172.90,202.90)		$-0.65^{+0.01}_{-0.01}$	$-2.18^{+0.01}_{-0.01}$	$466.80^{+5.28}_{-4.63}$	3799.78/360
(203.00,233.00)		$-0.85^{+0.09}_{-0.01}$	$-2.21^{+0.03}_{-0.05}$	$302.63^{+8.61}_{-6.83}$	1724.41/360
(233.10,263.10)		$-0.54^{+0.15}_{-0.23}$	$-1.70^{+0.05}_{-0.24}$	$454.01^{+271.34}_{-81.78}$	407.87/360
(172.90,202.90)	$35.00^{+0.55}_{-0.56}$	$-0.79^{+0.01}_{-0.01}$	$-2.40^{+0.02}_{-0.01}$	$744.88^{+11.34}_{-13.59}$	2745.70/360
(203.00,233.00)	$33.22^{+1.31}_{-1.10}$	$-1.06^{+0.02}_{-0.02}$	$-2.43^{+0.08}_{-0.11}$	$493.80^{+29.46}_{-26.01}$	1655.76/360

- 
37. Rau, A., Kienlin, A. V., Hurley, K., & Lichti, G. G., The 1st INTEGRAL SPI-ACS gamma-ray burst catalogue, *Astronomy and Astrophysics*. **438**,1175, (2005)
  38. Aptekar, R. L., et al., Konus-W Gamma-Ray Burst Experiment for the GGS Wind Spacecraft, *Space Science Reviews*. **71**,265, (1995)
  39. Hurley, K., et al., Mars Odyssey Joins the Third Interplanetary Network, *The Astrophysical Journal Supplement Series*. **164**,124, (2006)
  40. Castro-Tirado, A. J., Jelínek, M., Vítek, S., Kubánek, P., Trigo-Rodríguez, J. M., de Ugarte Postigo, A., Mateo Sanguino, T. J., & Gomboš, I., A very sensitive all-sky CCD camera for continuous recording of the night sky, *Advanced Software and Control for Astronomy II*. **7019**,70191V, (2008)
  41. Castro-Tirado, A. J., et al., The Burst Observer and Optical Transient Exploring System (BOOTES), *Astronomy and Astrophysics Supplement Series*. **138**,583, (1999) Castro-Tirado, A. J. et al., A very sensitive all-sky CCD camera for continuous recording of the night sky, in *Advanced Software and Control for Astronomy II*. Edited by Bridger, Alan; Radziwill, Nicole M. Proceedings of the SPIE, Volume 7019, article id. 70191V, 9 pp. (2008)
  42. Biryukov, A., Beskin, G., Karpov, S., Bondar, S., Ivanov, E., Katkova, E., Perkov, A., & Sasyuk, V., The first light of Mini-MegaTORTORA wide-field monitoring system, *Baltic Astronomy*. **24**,100, (2015)
  43. Karpov, S., et al., GRB 160625B: Mini-MegaTORTORA detection of bright optical flash simultaneous with LAT event., *GRB Coordinates Network*. **19603**,1, (2016)
  44. Cwiok, M., et al., Search for GRB related prompt optical emission and other fast varying objects with "Pi of the Sky" detector, *Astrophysics and Space Science*, **309**, 531, (2007).
  45. Mankiewicz, L., et al., Pi of the Sky full system and the new telescope, *RevMexAA (Serie de Conferencias)*, **45**, 7, (2014).
  46. Zarnecki, A.F., et al., Luiza: Analysis framework for GLORIA *Acta Polytechnica* **53(1)**, 5862, (2013)
  47. Zarnecki, A.F., et al., Analysis framework for GLORIA, *Proc. SPIE* **8454**, 845408, (2012)
  48. Cepa, J., et al., OSIRIS tunable imager and spectrograph, *Optical and IR Telescope Instrumentation and Detectors*. **4008**,623, (2000)



- 49. Schwarz, G., Estimating the Dimension of a Model, *Annals of Statistics*. **6**,461, (1978)
- 50. Kuroda, D., et al., GRB 160625B: MITSuME Ishigakijima Optical Observation., *GRB Coordinates Network*. **19599**,1, (2016)
- 51. Xu, D., Malesani, D., Fynbo, J. P. U., Tanvir, N. R., Levan, A. J.,& Perley, D. A., GRB 160625B: VLT/X-shooter redshift., *GRB Coordinates Network*. **19600**,1, (2016)